Femtosecond laser ablation of Cu_xZr_{1-x} bulk metallic glasses: A molecular dynamics study

Sébastien Marinier and Laurent J. Lewis*

Département de Physique and Regroupement Québécois sur les Matériaux de Pointe, Université de Montréal, Case Postale 6128 Succursale Centre-Ville, Montréal, Québec, Canada H3C 3J7

(Received 1 May 2015; revised manuscript received 20 August 2015; published 23 November 2015)

Molecular-dynamics simulations combined with a two-temperature model are used to study laser ablation in Cu_xZr_{1-x} ($x = 0.33, 0.50, 0.67$) metallic glasses as well as crystalline $CuZr_2$ in the $C11_b$ ($MoSi_2$) structure. Ablation thresholds are found to be 430 ± 10, 450 ± 10, 510 ± 10, and 470 ± 10 J/m$_2$ for a-Cu_2Zr, a-CuZr, a-$CuZr_2$, and c-$CuZr_2$, respectively. The larger threshold in amorphous $CuZr_2$ results from a weaker electron-phonon coupling and thus longer electron-ion equilibration time. We observe that the velocity of the pressure waves in the amorphous samples is not affected by the fluence, in contrast to the crystal; this is due to differences in the behavior of the shear modulus with increasing pressure. The heat-affected zone in the different systems is characterized in terms of the melting depth as well as inelastic deformations. The melting depth is found to be smaller in the crystal than in the amorphous targets because of its higher melting temperature. The inelastic deformations are investigated in terms of the von Mises shear strain invariant η^{Mises}; the homogeneous nucleation of shear transformation zones is observed in the glass as reported in previous theoretical and experimental studies. The coalescence of the shear transformation zones is also found at higher fluence.

DOI: 10.1103/PhysRevB.92.184108 PACS number(s): 61.80.Az, 61.82.Bg, 79.20.Eb

I. INTRODUCTION

Bulk metallic glasses (BMGs) have been the subject of numerous studies in the last few decades, largely because of their peculiar mechanical and magnetic properties, which make them attractive for numerous applications in various areas [1–7]. They generally possess high corrosion and wear resistance, high hardness, high strength, and fracture toughness, leading to applications in the fabrication of tools, anticorrosive and antiwear coatings, reflective coatings, sporting equipment, high-performance springs, medical devices, protection barriers for electronic components, etc. However, because of their higher hardness, conventional mechanical machining is less appropriate for these materials, and ultrashort laser pulse micromachining appears to be a promising avenue for carving out details on the submicron scale. This calls for a better understanding of the damage inflicted on the material by the laser pulses, as well as the characteristics of the ablation process. This is the object of the present paper.

There exist very few studies of laser ablation of glasses or disordered materials or studies that focus on the glassy/disordered nature of the targets. Some quaternary BMGs have been studied experimentally; it was found, for instance, that the ablation threshold is lower in the glassy state than in the crystalline state [8] for $Zr_{55}Al_{10}Ni_5Cu_{30}$ alloys and that laser ablation alters the magnetic properties of some Fe-based alloys [9]. Although in this work we focus on laser ablation, it is worth mentioning that laser welding of $Cu_{54}Ni_6Zr_{22}Ti_{18}$ [10,11] and $Zr_{55}Al_{10}Ni_5Cu_{30}$ [12] metallic glasses, along with pulsed laser deposition of Fe-Cr-Mo-Y-B-C on a steel substrate [13], has been investigated, but the ablation process *per se* was not studied. On the theoretical side, we are not aware of any studies of BMGs for laser ablation; however, molecular-dynamics (MD) simulations of the ablation of nanocrystalline aluminum [14] have been reported recently. A metallic glass can, in some sense, be viewed as the small-grain (atomic) limit of a nanocrystalline material, having a more homogeneous composition such that the possibility for the material to fracture at local defects or grain boundaries does not exist. Taking that into account, MD is a suitable tool for studying laser ablation in BMGs.

MD simulations have been successfully employed in the past to study laser ablation in different materials such as metals [15–19], organic materials [20–23], semiconductors [24], and nanocrystalline metals [14]. It was, in particular, used to investigate the mechanisms that lead to ablation [25–27], plume composition [28,29], laser-induced shock waves [30,31], defects [32–34], melting [35,36], and more. However, a comparison between the crystalline and glassy phases of a given material under laser ablation conditions has not been reported.

As BMGs do not respond to high pressure, high temperature, and probably fast energy deposition conditions the same way as crystalline metals do, we undertook characterization of laser ablation in the Cu-Zr binary metallic glass alloys and compare the result to a crystalline alloy of the same family. This system was chosen because it has been widely studied as a metallic glass [37–51], it has many crystalline phases depending on the atomic composition, and it has good glass-forming ability. Here, a two-temperature model (TTM) is used to describe the electronic properties of the system. This is coupled to a MD scheme so that the evolution of the material can be monitored, starting with the excitation of the electron gas and followed by the transfer of the energy to the ionic system which eventually leads to ablation.

The ablation threshold is found to be lower for the crystal than for the glass at a given composition. This is due to the fact that the electron-phonon equilibration time is larger for the amorphous sample because of its lower electron-phonon coupling. That influences cavitation, which is the mechanism that operates at the lowest fluences. The threshold, further, decreases with increasing Cu concentration as Cu atoms have a

*Author to whom correspondence should be addressed: Laurent.Lewis@UMontreal.CA

lower potential energy than Zr atoms. The velocity of the shock waves caused by the laser pulse increases with fluence in the crystal while it is almost constant in the glasses. This is directly related to the behavior of the shear modulus of the crystal with increasing pressure. We have also examined the heat-affected zone to better understand "collateral damage" resulting from the laser pulses; in particular, we investigate the melting depth and identify the zones where inelastic deformations appear after the passage of the shock waves. The nucleation of local shear transformation zones is observed in the glasses, and no clear inelastic deformations are found in the crystal. As a result, the damage is more important in the glasses than in the crystal.

II. COMPUTATIONAL DETAILS

A. Preparation and properties of samples

The Cu_xZr_{1-x} family of alloys forms glassy phases over a wide range of compositions (x between 0.25 and 0.70) [37,49]; this is advantageous as it makes identifying corresponding crystalline phases possible, which is important for the present study. To our knowledge, there are six stable Cu-Zr crystalline structures, viz., Cu_5Zr, $Cu_{51}Zr_{14}$, Cu_8Zr_3, $Cu_{10}Zr_7$, CuZr, and $CuZr_2$, as determined from experiment [39–41] and first-principles calculations [38]. Of the three structures with $0.25 \leqslant x \leqslant 0.70$, CuZr (B2) is not stable at temperatures lower than 988 K, and $Cu_{10}Zr_7$ forms a very complex structure which is not stable at 300 K with the interatomic potentials used in this work (see below); thus, $CuZr_2$ ($C11_b$) was used to compare with the glassy state for $x = 0.33$.

The glassy models at the various compositions of interest (we limited ourselves here to a-$CuZr_2$, a-CuZr, and a-Cu_2Zr) were prepared using a quench-from-the-melt procedure with MD simulations. In practice, we used the general-purpose LAMMPS MD package [52]. We start with a liquid at the proper composition ($x = 0.33$, 0.50, or 0.67) and equilibrated at 2000 K for 200 ps in the NPT ensemble, which we quench to 300 K at a cooling rate of 10^{11} K/s. This is then relaxed for 500 ps, still under NPT conditions, followed by 200 ps under NVT conditions, fixing the volume to the average equilibrium volume at 300 K. Ablation was carried out on the fully relaxed samples, all of which, including c-$CuZr_2$, contained 3.24×10^6 atoms, with the physical dimensions given in Table I. The targets are much longer in the z direction (normal to the surface, in the direction of the laser pulses), thick enough, in fact, that pressure waves resulting from the laser pulse, which would eventually get reflected on the back surface, will not interfere with the top surface before ablation is essentially complete. (Pressure-absorbing boundary conditions [53] at the bottom of the cell cannot be used here because they are not suitable for amorphous systems.) The lateral dimensions are much smaller than the thickness; as we impose periodic boundary conditions along the x and y directions, we are effectively considering an infinite surface, or to view it from another angle, we are considering a portion of the surface much smaller than the lateral dimensions of the laser pulses.

Figure 1 shows the partial and total radial distribution functions (RDFs) for the three amorphous samples after relaxation in the NVT ensemble. These show, among other things, that the second- and third-neighbor distances to each atom are shorter in a-Cu_2Zr than in the other two amorphous systems, while the first-neighbor distances are comparable, almost identical, as can, in fact, also be seen in Table I, where we also provide other characteristics of our systems, namely, the atomic density and the potential energies of Cu and Zr atoms. The calculated nearest-neighbor distances compare very well with those from experiment; indeed, Mattern *et al.* [49] obtained $R_{\text{Cu–Cu}} = 2.48$ Å, $R_{\text{Cu–Zr}} = 2.72$ Å, and $R_{\text{Zr–Zr}} = 3.12$ Å, independent of composition x. The difference between calculated and measured values, an acceptable ∼2%–4 %, reflects the limitations of our approach (empirical potentials used and fast cooling rates, for example).

B. Hybrid MD-TTM algorithm

A laser pulse impinges on the surface of a target and penetrates it to some extent; the photon energy is rapidly transferred to the electron gas (time scale of the order of several femtoseconds) which itself "slowly" transfers energy to the ion gas by way of the electron-phonon coupling (time scale of the order of several picoseconds). The dynamics of the target is here modeled using a combined MD-TTM scheme [15,54], which provides the essential connection between the electron and the ion gas, subject to the influence of a "source" of excitation. We thus have

$$C_e(T_e,\rho)\frac{\partial T_e}{\partial t} = \nabla[\kappa_e(T_e,T_i,\rho)\nabla T_e] - \Gamma(T_e,T_i,\rho)(T_e - T_i) + Q(\mathbf{r},t), \quad (1)$$

where T_e and T_i are the electronic and ionic temperatures, respectively, ρ is the ionic density, C_e is the electronic specific heat, κ_e is the electronic thermal conductivity, G is the electron-ion coupling constant, and $Q(\mathbf{r},t)$ is the source, here the laser pulse. We assume that the pulse has a Gaussian temporal profile of width $\tau_L = 2\sigma = 200$ fs and spatially obeys the Beer-Lambert-Bouguer law in the pulse direction (z) at current time t and position $\mathbf{r}$ within the target. Equation (1) is treated as an additional force acting on the ions and is integrated within the MD algorithm using a finite-volume scheme, which resolves the "ionic" part of the TTM [15]. The direct interactions

TABLE I. Lateral dimensions ($\ell_x = \ell_y = \ell_{x,y}$), thickness ℓ_z, equilibrium density ρ_0, potential energy E_i^0 (i = Cu and Zr), and nearest-neighbor distances R_{i-j} for the different samples. (The latter are not given for the crystal since they cannot be directly compared to those for the amorphous phase; see text for details.)

	Sample			
	c-$CuZr_2$	a-$CuZr_2$	a-CuZr	a-Cu_2Zr
ℓ_{xy} (nm)	9.721	9.906	9.479	9.091
ℓ_z (nm)	657.1	645.3	633.5	615.9
ρ_0 (10^{28} atoms/m^3)	5.1438	5.1166	5.6924	6.3648
E^0_{Cu} (eV/atom)	−3.46	−3.44	−3.42	−3.37
E^0_{Zr} (eV/atom)	−6.47	−6.32	−6.32	−6.28
$R_{\text{Cu–Cu}}$ (Å)		2.57	2.58	2.57
$R_{\text{Cu–Zr}}$ (Å)		2.77	2.78	2.80
$R_{\text{Zr–Zr}}$ (Å)		3.18	3.20	3.22

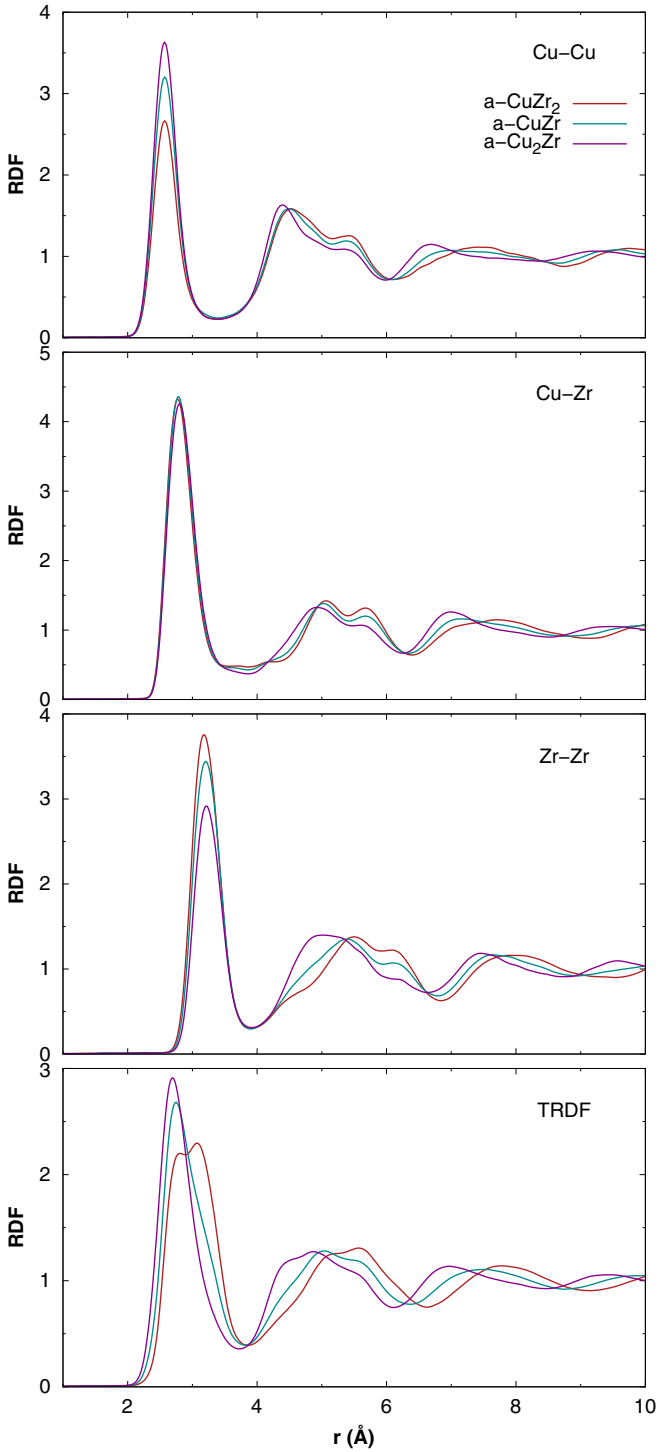

FIG. 1. (Color online) Partial radial distribution functions for Cu-Cu, Cu-Zr, and Zr-Zr interatomic distance along with the total radial distribution function (TRDF) for the three amorphous samples.

between ions are described in terms of the Finnis-Sinclair embedded-atom method potential (EAM/FS) [55,56] fitted by Mendelev *et al.* [57] as it provides an appropriate description of the properties of liquid and amorphous Cu_xZr_{1-x} alloys. The $C11_b$ ($MoSi_2$) crystalline structure can be described by multiple lattice constants, as shown in Fig. 2. Using equilibrium NVT simulations at $T = 300$ K, we obtained

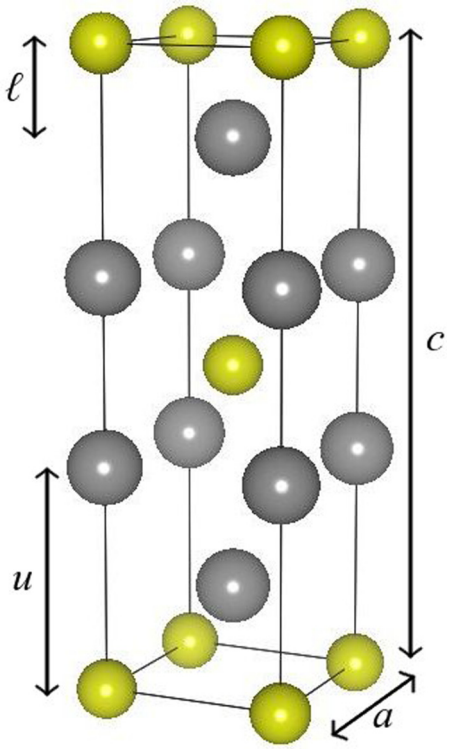

FIG. 2. (Color online) $C11_b$ structure for crystalline $CuZr_2$ showing the four lattice parameters a, c, u, and ℓ.

$a = 3.2398$ Å, $c = 10.9496$ Å, $u = 0.353c$, and $\ell = 0.147c$, leading to a minimum in potential energy for this structure. This compares reasonably well with experiment [58]: $a = 3.2204$ Å and $c = 11.183$ Å, so that $c/a = 3.473$ vs 3.3797 in our model; the constants u and ℓ were not reported.

The TTM requires several parameters which are not necessarily easy to obtain for alloys. First, the discrete Beer-Lambert-Bouguer law involves an optical absorption coefficient $\alpha = 1/\delta_L$, with δ_L being the optical penetration length of the laser in the material. Here, we assume that α depends linearly on concentration, $\alpha_x = x\alpha_{Cu} + (1-x)\alpha_{Zr}$, where α_i is the absorption coefficient for the crystalline species Cu and Zr. For Cu, $1/\alpha = 12.2$ nm (for a wavelength $\lambda_0 = 826$ nm, typical of a Ti:sapphire laser) [59]; for Zr we used

$$\alpha = \frac{4\pi\tilde{k}}{\lambda_0}, \tag{2}$$

where $\tilde{k}$ is the extinction coefficient [60], whose value is 4.0 for Zr, yielding $1/\alpha = 16.4$ nm. While our model for α might be a bit crude, we have verified that the results are not oversensitive to the value of the wavelength.

The Sommerfeld approximation was used for the electronic specific heat, $C_e(T_e,\rho) = \gamma T_e \rho^*$, where ρ^* is the reduced ionic density (ρ/ρ_0) and γ is a constant which depends on the material. The electronic specific heat of Cu-Zr binary alloys in glassy and crystalline forms has been studied by Garoche and Bigot [61]; the values of γ for our different systems are reported in Table II. As for the electronic contribution to the

TABLE II. Specific-heat constant γ, coupling-constant ratio χ, e-e and e-ph collision rate parameters A and B, Fermi energy E_F, and optical penetration depth $1/\alpha$ for all the samples.

Target	γ (J m^{-3} K^{-2})	χ	A (10^6 K^{-2} s^{-1})	B (10^{12} K^{-1} s^{-1})	E_F (eV)	$1/\alpha$ (nm)
c-$CuZr_2$	194.2	1.0	4.45	3.50	1.0	14.8
a-$CuZr_2$	384.7	0.56	4.45	3.50	1.0	14.8
a-CuZr	321.3	0.98	1.86	2.64	1.4	14.0
a-Cu_2Zr	289.6	1.04	8.69	1.79	2.0	13.3

thermal conductivity, we used the Drude model:

$$\kappa_e(T_e,T_i) = \tfrac{1}{3}\bar{v}^2 C_e(T_e,\rho)\tau_e(T_e,T_i). \quad (3)$$

Here, $\bar{v}^2$ is the mean-square velocity of the electrons contributing to the thermal conductivity, and $\tau_e(T_e,T_i)$ is the total electron scattering time. The mean-square velocity can be approximated, as Inogamov and Petrov [62] suggested, by

$$\bar{v^2} = \sqrt{\left(\frac{6E_F}{5m_e}\right)^2 + \left(\frac{3k_BT_e}{m_e}\right)^2}, \quad (4)$$

where E_F is the Fermi energy and m_e is the electron mass. The Fermi energy for the amorphous samples was taken from the literature [63]; since Zr d electrons, which are responsible for the conductivity, are only slightly affected by the structure, we used the same value for both amorphous and crystalline $CuZr_2$ samples. The electron scattering time is obtained from $\tau_e^{-1} = AT_e^2 + BT_i$, where the first term is the electron-electron scattering rate τ_{e-e}^{-1} and the second term is the electron-phonon scattering rate τ_{e-ph}^{-1}. The values for A and B were approximated by $A(Cu_xZr_{1-x}) = xA_{Cu} + (1-x)A_{Zr}$ and $B(Cu_xZr_{1-x}) = xB_{Cu} + (1-x)B_{Zr}$. For Cu, we have [59] $A = 1.23 \times 10^7$ $K_{-2}s_{-1}$ and $B = 1.28 \times 10^{11} K_{-1}s_{-1}$. For Zr, we used the random-phase approximation [64] to get $A = 3.41 \times 10^5 K_{-2}s_{-1}$; from the Wiedemann-Franz law and electrical resistivity data [65], we get $B = 5.16 \times 10^{12} K_{-2}s_{-1}$.

According to Lin *et al.* [66], the electron-phonon coupling parameter can be approximated by

$$\Gamma(T_e) = \frac{\pi\hbar k_B \Lambda\langle\omega^2\rangle}{g(E_F)} \int_{-\infty}^{\infty} g^2(\varepsilon)\left(-\frac{\partial f}{\partial \varepsilon}\right)d\varepsilon, \quad (5)$$

where Λ is the mass enhancement parameter, $\langle\omega^2\rangle$ is the second moment of the phonon spectrum [67], $g(\varepsilon)$ and $g(E_F)$ are the electron densities of states at energy ε and at the Fermi energy, respectively, and $f(\varepsilon)$ is the Fermi function. This has already been tabulated [66] for Cu but not for Zr. One can approximate $\hbar^2\langle\omega^2\rangle \sim k_B^2\theta_D^2$, and using $\Lambda = 0.55$ [68], we integrate the electron density of states of Zr to obtain the electron-phonon coupling parameter as a function of the electronic temperature. As discussed by Garoche and Bigot [61], we can write the ratio of electron-phonon coupling parameters for amorphous and crystalline alloys for a given value of x as

$$\chi = \frac{\Gamma_a}{\Gamma_c} = \frac{g_c^0 E_a^0}{g_a^0 E_c^0}, \quad (6)$$

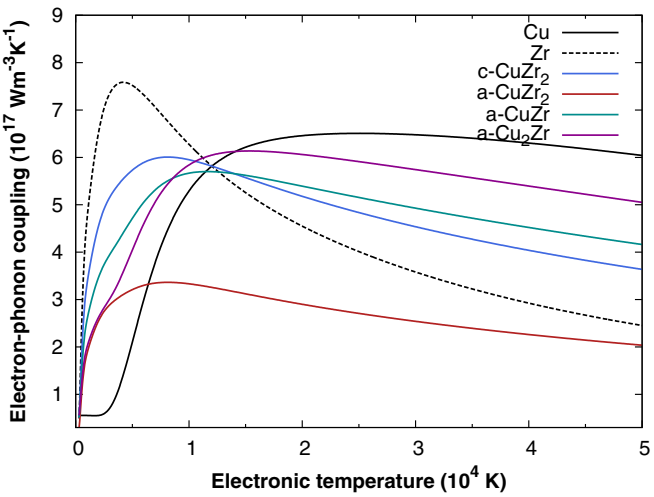

FIG. 3. (Color online) Electron-phonon coupling parameter as a function of electronic temperature for all the targets along with pure Cu and Zr.

where Γ_c, Γ_a, g_c^0, g_a^0, E_c^0, and E_a^0 are the electron-phonon coupling parameters, electronic densities of states at the Fermi level, and equilibrium energies for crystalline (c) and amorphous (a) states, respectively. We approximated the electron-phonon coupling parameter for a-Cu_xZr_{1-x} by $\Gamma_x^a(T_e) = \chi_x[x\Gamma_{Cu}(T_e) + (1-x)\Gamma_{Zr}(T_e)]$, with χ being equal to 1 for the crystalline state. The electron-phonon coupling parameters for the different amorphous and crystalline alloys, along with those for pure Cu and Zr, are shown in Fig. 3 as a function of the electronic temperature. The coupling constant for $CuZr_2$ is lower in the glassy state than in the crystalline state due to a higher electronic density of states. The different parameters for the TTM-MD algorithm are presented in Table II for all samples.

III. RESULTS AND DISCUSSION

A. Ablation yield and threshold

Depending on the laser fluence, many different mechanisms may occur during the ablation process [26]. The ablation threshold F_{th} is the fluence at which massive (collective) ejection of matter takes place; depending on the value of F_{th}, the fluence is "low" or "high," with or without plasma effects. Figure 4 shows the total ejected mass per area unit ("yield") as a function of fluence for the different targets. From this graph we obtain threshold fluences of 430 ± 10, 450 ± 10, 510 ± 10, and 470 ± 10 J/m_2 for a-Cu_2Zr, a-CuZr, a-$CuZr_2$, and c-$CuZr_2$, respectively. The higher ablation threshold for a-$CuZr_2$ is the consequence of a lower electron-phonon coupling compared to the other systems (see Fig. 3), which implies that the electron-phonon equilibration time is longer in this case, as can, indeed, be seen in Fig. 5. The equilibration time (or characteristic time) is defined here as the time required for E_k^e to drop to $E_{abs}/3$, where E_k^e is the total kinetic energy of the electrons in the system and E_{abs} is the total energy absorbed from the laser. This quantity provides an estimate of the time required for the electronic and ionic temperatures to equilibrate in the bulk (which can be very long compared to

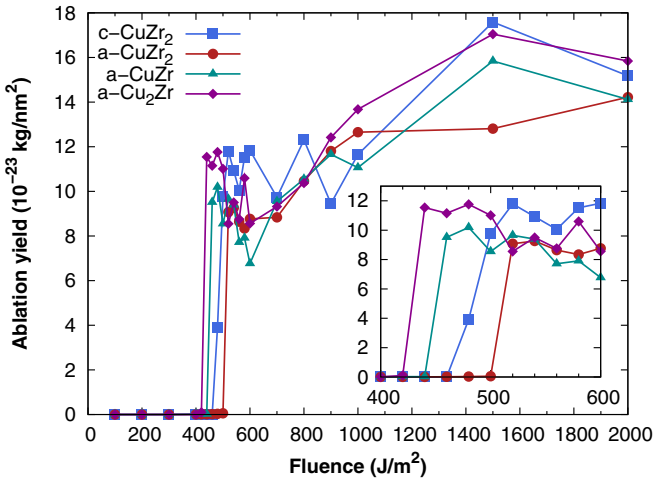

FIG. 4. (Color online) Ejected mass per area unit as a function of the laser fluence for each of the four targets. The inset is a zoom of the region [400 : 600] J/m_2.

the time covered by the simulations). The larger equilibration time in a-$CuZr_2$ leads to less intense pressure waves following irradiation, thus to weaker pressure gradients, which explains the higher ablation threshold in this system.

Cavitation is the ablation mechanism that operates at the lowest fluence and hence determines the ablation threshold. It is therefore instructive to better understand how it is affected by the laser pulse. In this regard, we examined how the intensities of both the compressive and tensile waves evolve with increasing fluence. Figures 6(a) and 6(b) show the maximum values of the tensile and the compressive wave (averaged over the first 50 ps), respectively, for the different targets as a function of fluence. Near the ablation threshold, the maximum tension is lower in a-$CuZr_2$ than in other samples, which explains the higher ablation threshold as noted above. In addition, the highest value of the maximum tension occurs at a fluence slightly below F_{th} due to the fact that part of the tension is "absorbed" by the cavities that ultimately lead to ablation

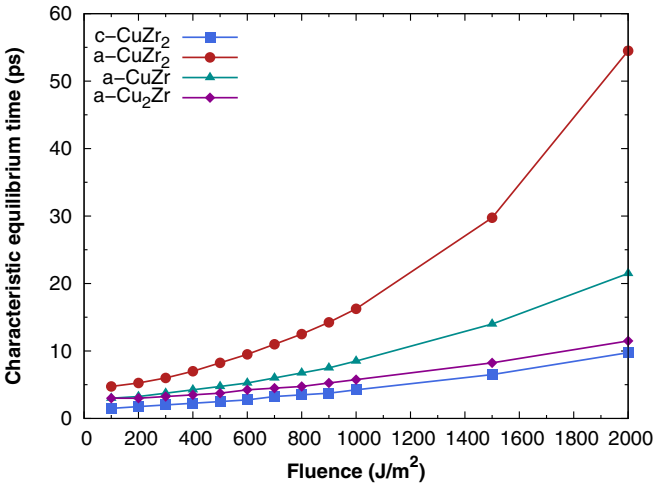

FIG. 5. (Color online) Electron-phonon equilibration time as a function of fluence for the four samples; see text for details.

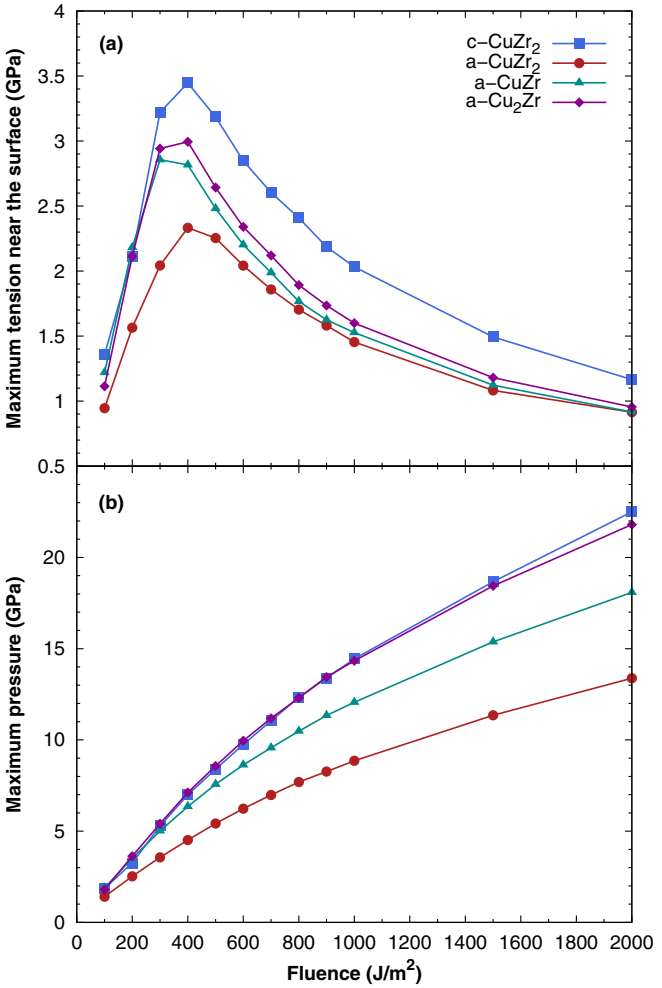

FIG. 6. (Color online) (a) Maximum tension near the surface and (b) maximum pressure of the different samples as a function of fluence.

(cavitation). This also clarifies why the tension decreases at fluences above F_{th}. To conclude on this point, the ablation threshold is larger in the glass than in the crystal (a-$CuZr_2$ vs $CuZr_2$) because of its lower electron-phonon coupling, which leads to more intense tensile waves.

We now turn to the effect of atomic concentration x on the ablation yield in the glassy state. As can be seen in Fig. 4, higher Cu concentrations lead to higher yields at high fluence, which means that higher-fluence mechanisms such as fragmentation and vaporization [26] are more present in the cases of a-CuZr and a-Cu_2Zr. Those two high-fluence mechanisms produce smaller clusters of atoms (vaporization producing a gas and fragmentation yielding very small liquid droplets in a gas), which means that the yield for a small cluster (diameter $d \leqslant 3$ nm) should also be higher in those samples. We have verified this as shown in Fig. 7, where we plot the yield for small clusters as a function of fluence. For fluences larger than 1000 J/m_2, this is higher not only for a-CuZr and a-Cu_2Zr but also for c-$CuZr_2$. This figure also demonstrates that high-fluence mechanisms are more active in the crystal than in the glass at a given concentration.

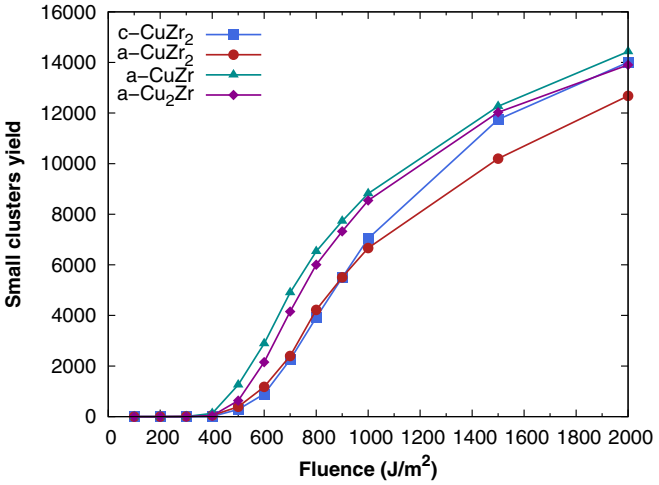

FIG. 7. (Color online) Number of clusters with $d \leqslant 3$ nm as a function of fluence for the various samples.

B. Shock waves

Figure 8 presents the velocity of propagation of pressure waves in the samples as a function of fluence. These were calculated using simply $\Delta x(p_{\max})/\Delta t$ at different times, then averaging over the first 80 ps in order to eliminate the interference caused by the reflected wave (owing to the finite size of the sample). For illustration purposes, a spatial pressure profile is shown in Fig. 9 for the crystalline and amorphous $CuZr_2$ samples at 600 J/m_2; evidently, the velocity of the pressure waves changes only slightly with time, so that taking a simple average is sufficiently accurate.

From Fig. 8 we see that the faster a pressure wave travels, the higher the strain rate is, eventually leading to cavitation and material fracture. The pressure waves travel much faster in the crystalline sample than in all amorphous ones, and this effect amplifies with increasing fluence: ∼1000 m/s and more quickly for fluences larger than 800 J/m_2. For the glassy state, the propagation velocity does not depend much on fluence, but it does for the crystalline sample, especially for fluences lower

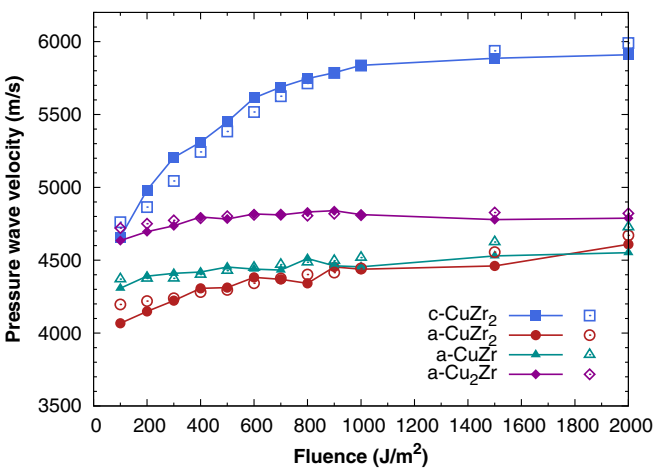

FIG. 8. (Color online) Mean pressure-wave velocity in the samples as a function of fluence. Connected solid dots are values from the simulations, and empty dots are values calculated by Eq. (7).

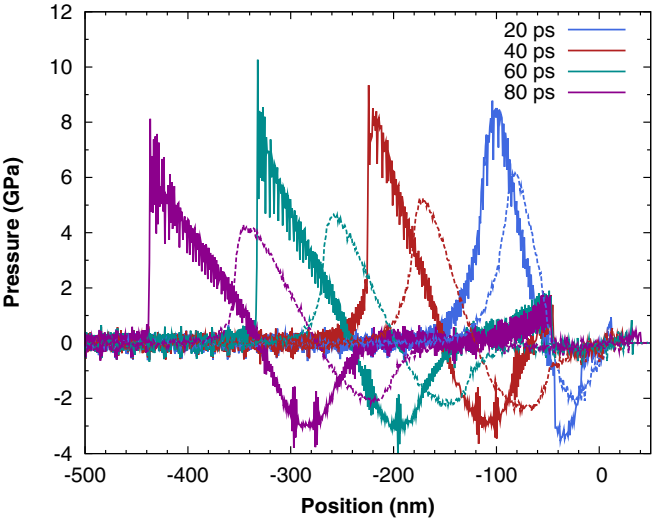

FIG. 9. (Color online) Spatial pressure profile for crystalline (solid lines) and amorphous (dashed lines) $CuZr_2$ at different times and at a fluence of 600 J/m_2. The initial surface is at position $z = 0$ nm.

than 800 J/m_2. The pressure-wave velocity in homogeneous and isotropic mediums is calculated by

$$v_p(p) = \sqrt{\frac{K(p) + \frac{4}{3}G(p)}{\rho(p)}}, \tag{7}$$

where K is the bulk modulus, G is the shear modulus, and ρ si the density, which all depend on pressure p. Given that the bulk modulus and the density increase only slightly with pressure, we infer that it is the behavior of $G(p)$ that determines the dependence of v_p on pressure and hence fluence since the maximum pressure in the samples, shown in Fig. 6(b), increases with fluence. We have calculated the shear modulus by uniaxially compressing the samples along the z axis (i.e., parallel to the direction of the pulse). The results are shown in Fig. 10. As expected, the shear modulus initially increases

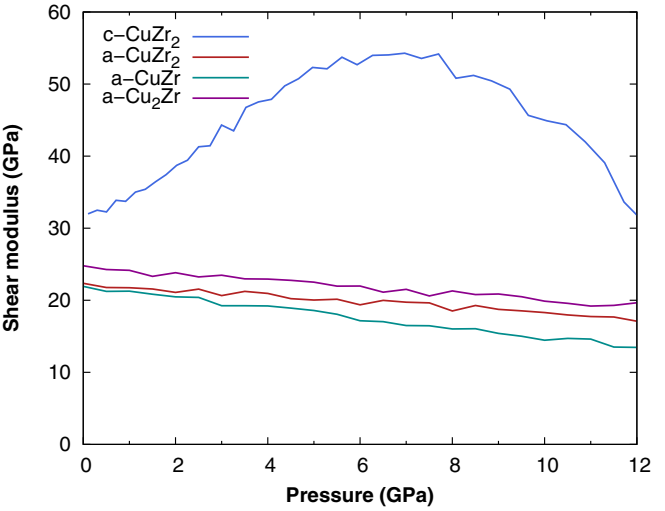

FIG. 10. (Color online) Shear modulus as a function of pressure for the different samples.

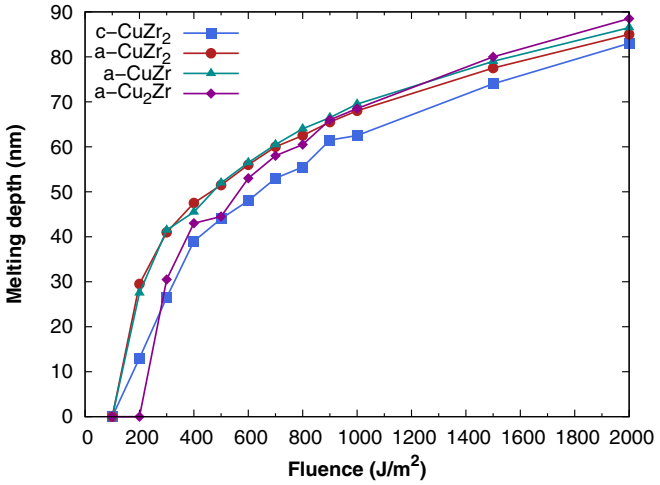

FIG. 11. (Color online) Melting depth vs fluence for the different samples.

with pressure for the crystal, then decreases as the material reaches its elastic limit. As for the glassy samples, G slowly decreases with increasing pressure. Returning to Fig. 8, we also compare the values of the pressure-wave velocity from the simulations to those from Eq. (7); this indeed confirms that it is the behavior of $G(p)$ that contributes to the velocity increase at lower fluences for the crystal. The higher pressure-wave velocity combined with the faster energy deposition in the ionic system thus explains the lower ablation threshold for a-$CuZr_2$ versus c-$CuZr_2$, as the pressure gradient is higher and operates at a faster pace in the crystal.

C. Heat-affected zone

We now evaluate the damage inflicted on the targets by the laser pulses, more specifically in the so-called heat-affected zone (HAZ). This is defined as the region where permanent changes appear. Here, we focus on the melted region and the plastically deformed region. Figure 11 shows the melting depth as a function of fluence for all four samples. There is not a large difference between the targets as far as the molten region is concerned, considering also that the uncertainty is about ± 5 nm on each data point (which arises from the finite thickness of the solid-liquid interface, between 5 and 10 nm). However, it is clear that the melting depth in the crystalline sample is smaller than in the amorphous samples, at least above the ablation threshold. This is due to the fact that the melting temperature T_m for c-$CuZr_2$ is 1750 ± 10 K with the interatomic potentials used, substantially larger than for the amorphous samples, viz., 1200 ± 10, 1210 ± 10, and 1300 ± 10 K for a-$CuZr_2$, a-CuZr, and Cu_2Zr, respectively. Those values of T_m were obtained from several NPT simulations, each 250 ps long, at different values of T. For the crystal, T_m is defined as the temperature at which the latent heat is released; that is, a strong increase in the potential energy is observed. As for the amorphous samples, the melting temperature is defined as the temperature at which the mean-square displacement drastically increases and the density is the same as the melted crystal (for the same temperature); we note that no significant crystallization was observed in the amorphous samples.

In BMGs, plastic deformations are caused by small localized irreversible shear strain regions called shear transformation zones (STZs), which appear when the material undergoes a large enough shear stress [69,70]. Because glasses do not possess preexisting defects, there is no way to predict where these zones will develop. Consequently, plastic deformations in BMGs originate from homogeneous nucleation of STZs. When the shear stress is large enough in the material, STZs may diffuse and coalesce into shear bands, which literally are bands created by merged STZs. With increasing shear stress, those bands eventually form shear cracks, leading to the rupture of the material. Considering that the laser pulse generates a pressure wave and possibly high-stress regions, it is relevant to look for nucleation of STZs in the amorphous samples.

A convenient quantity [71] for characterizing shear flow in amorphous metals is the von Mises shear-strain parameter η^{Mises}, which possesses a value for each atom i in the sample. This is defined by comparing the configuration at some time after the beginning of the simulation to a reference configuration, which is the initial relaxed configuration. The number of nearest neighbors of atom i in the reference configuration is denoted n_i^0. We define vectors $\mathbf{d}_{ij}$ separating atom i from each of its neighbors j, and these are labeled $\mathbf{d}_{ij}^0$ in the reference configuration. For each atom i, an affine transformation matrix $\mathbf{J}_i$ minimizing $\sum_j |\mathbf{d}_{ji}^0 \mathbf{J}_i - \mathbf{d}_{ji}|^2$ is constructed. The purpose of this matrix is to map all the transformations $\{\mathbf{d}_{ji}^0\} \longrightarrow \{\mathbf{d}_{ji}\}$ for all the nearest neighbors j, so that in the absence of shear strain, the above sum would be zero. With this transformation matrix, the strain matrix is defined as

$$\boldsymbol{\eta}_i = \tfrac{1}{2}\left(\mathbf{J}_i \mathbf{J}_i^{\mathrm{T}} - \mathbf{I}\right), \tag{8}$$

where $\mathbf{I}$ is the identity matrix. The von Mises strain for atom i can then be calculated using

$$\eta_i^{\text{Mises}} = \left\{\tfrac{1}{6}\left[(\eta_{11}-\eta_{22})^2 + (\eta_{22}-\eta_{33})^2 + (\eta_{33}-\eta_{11})^2\right] + \eta_{12}^2 + \eta_{23}^2 + \eta_{31}^2\right\}^{1/2}, \tag{9}$$

where $\eta_{\alpha\beta}$ are the matrix elements of the strain matrix $\boldsymbol{\eta}$. This expression can be described as the local deviation from the affine transformation that would be mapped by $\mathbf{J}_i$ in the absence of shear strain, in which case $\eta_i^{\text{Mises}} = 0$ for all atoms i.

Figure 12 shows the nucleation of STZs in the amorphous $CuZr_2$ sample for fluences of 600 J/m_2 and 2000 J/m_2. At the higher fluence, coalescence of STZs can be observed, although it is not clear if shear banding is present on this time scale. For the lower fluence, no merging of STZs is observed as there are only small localized STZs in the sample. Corresponding results for a-CuZr and a-Cu_2Zr show that the STZs are slightly larger when the copper content increases, but no obvious shear banding is observed because the shear stress induced by the laser is not strong enough to allow this; thus, even at high fluence ($\sim 3F_{\text{th}}$), there is no shear flow in the metallic glass. For the crystalline sample, small plastic deformations are observed at high fluence near the melting front, which is likely a consequence of residual stress. Those small plastic deformations extend the HAZ by about 10 nm at 1500 and 2000 J/m_2.

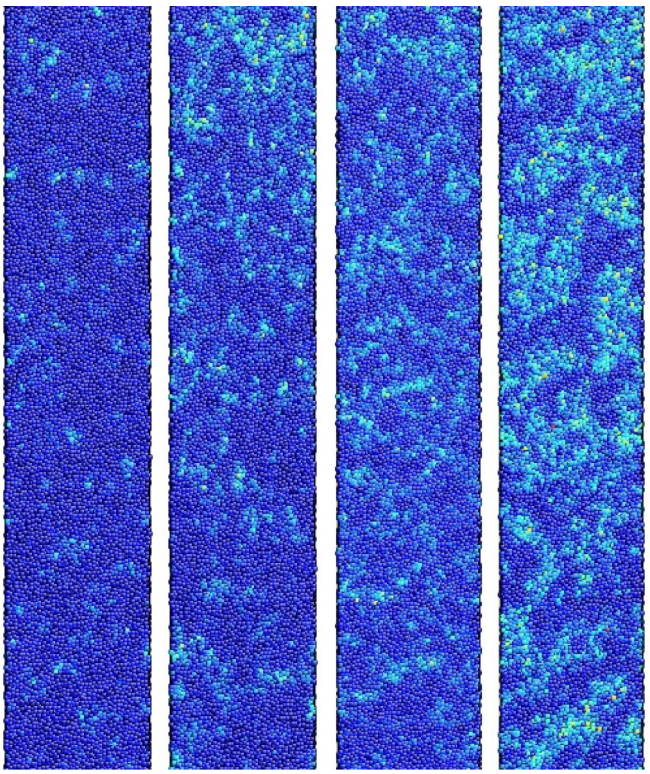

(a) 40 ps (b) 250 ps (c) 40 ps (d) 250 ps

FIG. 12. (Color online) STZ nucleation in the glassy $CuZr_2$ sample at different times for a fluence of (a) and (b) 600 J/m_2 and (c) and (d) 2000 J/m_2. Atoms are colored according to the value of η_i^{Mises} from 0 (blue) to 0.6 (red).

IV. CONCLUSION

Using a TTM-MD scheme, we have investigated the laser ablation of $Cu_xZr_{1-x}(x = 0.33, 0.50, 0.67)$ metallic glasses as well as crystalline $CuZr_2$ in the $C11_b$ ($MoSi_2$) structure. As only a very few experiments have been reported on this particular problem, this study is both timely and relevant. We have studied how disorder in a binary metallic alloy affects ablation. We have found that the ablation threshold is slightly higher in the amorphous $CuZr_2$ sample than in the other samples because of its smaller electron-phonon coupling parameter, which makes the equilibration time longer and thus leads to lower pressure-wave intensities in the bulk. The pressure-wave velocity increases with the laser fluence in the crystalline sample but not in the glasses, where it is roughly constant. This is explained by the behavior of the shear modulus with increasing pressure. The heat-affected zone has been characterized in terms of the melting depth as well as plastic deformations in all samples. The melting depth is generally smaller in the crystal than in the glasses as the melting temperature is significantly higher. No plastic deformations were clearly observed in the crystal except near the melting front at high fluence, which is related to residual stresses. In the amorphous samples, homogeneous nucleation of STZs has been observed as predicted. At high fluence ($\sim$2–3F_{th}), STZ diffusion and merging have been observed, but no shear banding occurs, likely because the shear stresses caused by the laser pulses are too weak for this to happen. Consequent to those last results, the HAZ is smaller in the crystalline sample than in the glassy samples, and so the damage from laser ablation is less important in the crystal than in the metallic glass.

Looking beyond the present study, knowledge of the ρ-T or p-T phase diagrams for Cu_xZr_{1-x} in the amorphous and/or crystalline phases, which is a difficult problem, would allow the thermodynamic trajectories to be calculated and thus to determine precisely the thermal ablation mechanisms, thus offering an even better comprehension of how this material is affected by femtosecond laser pulses. It would be interesting to see if a mechanical fracture in the solid part of the metallic glass at higher fluences could eventually be observed. This would set the table for some experiments on metallic glasses and their crystalline counterparts and even further theoretical studies on disordered materials and their interaction with lasers. For example, how would plastically deformed metallic glasses react to multiple pulses, or how is the HAZ affected by the pulse duration? This is a matter for future studies.

ACKNOWLEDGMENTS

We are grateful to M. Gill-Comeau and N. Tsakiris for useful discussions. This work has been supported by grants from the Natural Sciences and Engineering Research Council of Canada (NSERC) and the Fonds de Recherche du Québec—Nature et Technologies (FRQNT). We are indebted to Calcul Québec and Calcul Canada for generous allocations of computer resources.

[1] P. Chaudhari and D. Turnbull, Science **199**, 11 (1978).
[2] J. F. Löffler, Intermetallics **11**, 529 (2003).
[3] W.-H. Wang, C. Dong, and C. Shek, Mater. Sci. Eng. R **44**, 45 (2004).
[4] A. R. Yavari, J. Lewandowski, and J. Eckert, MRS Bulletin **32**, 635 (2007).
[5] R. Cahn, Contemp. Phys. **21**, 43 (1980).
[6] M. Miller and P. Liaw, *Bulk Metallic Glasses* (Springer, New York, 2008).
[7] C. Suryanarayana and A. Inoue, *Bulk Metallic Glasses* (CRC Press, Boca Raton, 2011).
[8] T. Sano, K. Takahashi, A. Hirose, and K. F. Kobayashi, Mater. Sci. Forum **539-543**, 1951 (2007).
[9] M. Sorescu, L. Tsakalakos, and T. Sands, J. Appl. Phys. **85**, 6652 (1999).
[10] J. Kim, D. Lee, S. Shin, and C. Lee, Mater. Sci. Eng. A **434**, 194 (2006).
[11] J. H. Kim, C. Lee, D. Lee, J. Sun, S. Shin, and J. Bae, Mater. Sci. Eng. A **449**, 872 (2007).
[12] Y. Kawahito, T. Terajima, H. Kimura, T. Kuroda, K. Nakata, S. Katayama, and A. Inoue, Mater. Sci. Eng. B **148**, 105 (2008).

[13] A. Basu, A. Samant, S. Harimkar, J. D. Majumdar, I. Manna, and N. B. Dahotre, Surf. Coat. Technol. **202**, 2623 (2008).
[14] M. Gill-Comeau and L. J. Lewis, Phys. Rev. B **84**, 224110 (2011).
[15] D. S. Ivanov and L. V. Zhigilei, Phys. Rev. B **68**, 064114 (2003).
[16] N. Nedialkov, S. Imamova, P. Atanasov, P. Berger, and F. Dausinger, Appl. Surf. Sci. **247**, 243 (2005).
[17] N. Nedialkov, S. Imamova, and P. Atanasov, J. Phys. D **37**, 638 (2004).
[18] C. Schäfer, H. M. Urbassek, and L. V. Zhigilei, Phys. Rev. B **66**, 115404 (2002).
[19] C. Cheng and X. Xu, Phys. Rev. B **72**, 165415 (2005).
[20] L. V. Zhigilei, P. B. Kodali, and B. J. Garrison, J. Phys. Chem. B **101**, 2028 (1997).
[21] L. V. Zhigilei and B. J. Garrison, Appl. Phys. Lett. **74**, 1341 (1999).
[22] L. V. Zhigilei, P. Kodali, and B. J. Garrison, Chem. Phys. Lett. **276**, 269 (1997).
[23] L. V. Zhigilei and B. J. Garrison, J. Appl. Phys. **88**, 1281 (2000).
[24] P. Lorazo, L. J. Lewis, and M. Meunier, Phys. Rev. B **73**, 134108 (2006).
[25] D. Perez and L. J. Lewis, Phys. Rev. Lett. **89**, 255504 (2002).
[26] D. Perez and L. J. Lewis, Phys. Rev. B **67**, 184102 (2003).
[27] P. Lorazo, L. J. Lewis, and M. Meunier, Phys. Rev. Lett. **91**, 225502 (2003).
[28] M. I. Zeifman, B. J. Garrison, and L. V. Zhigilei, J. Appl. Phys. **92**, 2181 (2002).
[29] L. Zhigilei, Appl. Phys. A **76**, 339 (2003).
[30] J. A. Smirnova, L. V. Zhigilei, and B. J. Garrison, Comput. Phys. Commun. **118**, 11 (1999).
[31] B. Arman, S.-N. Luo, T. C. Germann, and T. Çağın, Phys. Rev. B **81**, 144201 (2010).
[32] D. Bouilly, D. Perez, and L. J. Lewis, Phys. Rev. B **76**, 184119 (2007).
[33] Z. Lin, R. A. Johnson, and L. V. Zhigilei, Phys. Rev. B **77**, 214108 (2008).
[34] L. V. Zhigilei and B. J. Garrison, Appl. Surf. Sci. **127**, 142 (1998).
[35] M. D. Kluge, J. R. Ray, and A. Rahman, J. Chem. Phys. **87**, 2336 (1987).
[36] S. Kotake and M. Kuroki, Int. J. Heat Mass Transfer **36**, 2061 (1993).
[37] Z. Altounian, T. Guo-hua, and J. Strom-Olsen, J. Appl. Phys. **53**, 4755 (1982).
[38] G. Ghosh, Acta Mater. **55**, 3347 (2007).
[39] H. Okamoto, J. Phase Equilib. Diffus. **29**, 204 (2008).
[40] D. Arias and J. P. Abriata, Bulletin of Alloy Phase Diagrams **11**, 452 (1990).
[41] *Phase Diagrams of Binary Copper Alloys*, Monograph Series on Alloy Phase Diagrams, edited by P. R. Subramanian, Vol. 10 (ASM International, Materials Park, 1994).
[42] D. Xu, B. Lohwongwatana, G. Duan, W. L. Johnson, and C. Garland, Acta Mater. **52**, 2621 (2004).
[43] T. Mei-Bo, Z. De-Qian, P. Ming-Xiang, and W. Wei-Hua, Chin. Phys. Lett. **21**, 901 (2004).
[44] T. Fukunaga, K. Itoh, T. Otomo, K. Mori, M. Sugiyama, H. Kato, M. Hasegawa, A. Hirata, Y. Hirotsu, and A. Hannon, Intermetallics **14**, 893 (2006).
[45] P. Oelhafen, E. Hauser, H.-J. Güntherodt, and K. H. Bennemann, Phys. Rev. Lett. **43**, 1134 (1979).
[46] G. Duan, D. Xu, Q. Zhang, G. Zhang, T. Cagin, W. L. Johnson, and W. A. Goddard, III, Phys. Rev. B **71**, 224208 (2005).
[47] Q. Zhang, W. Zhang, and A. Inoue, Scr. Mater. **55**, 711 (2006).
[48] X. Wang, S. Yin, Q. Cao, J. Jiang, H. Franz, and Z. Jin, Appl. Phys. Lett. **92**, 011902 (2008).
[49] N. Mattern, A. Schöps, U. Kühn, J. Acker, O. Khvostikova, and J. Eckert, J. Non-Cryst. Solids **354**, 1054 (2008).
[50] N. Mattern, J. Bednarčik, S. Pauly, G. Wang, J. Das, and J. Eckert, Acta Mater. **57**, 4133 (2009).
[51] N. Mattern, P. Jovari, I. Kaban, S. Gruner, A. Elsner, V. Kokotin, H. Franz, B. Beuneu, and J. Eckert, J. Alloys Compd. **485**, 163 (2009).
[52] S. Plimpton, J. Comput. Phys. **117**, 1 (1995).
[53] C. Schäfer, H. M. Urbassek, L. V. Zhigilei, and B. J. Garrison, Comput. Mater. Sci. **24**, 421 (2002).
[54] S. I. Anisimov, B. L. Kapeliovich, and T. L. Perel'man, Zh. Eksp. Teor. Fiz. **66**, 776 (1974).
[55] M. S. Daw and M. I. Baskes, Phys. Rev. B **29**, 6443 (1984).
[56] M. Finnis and J. Sinclair, Philos. Mag. A **50**, 45 (1984).
[57] M. Mendelev, M. Kramer, R. Ott, D. Sordelet, D. Yagodin, and P. Popel, Philos. Mag. **89**, 967 (2009).
[58] L. A. Mendoza-Zélis, L. C. Damonte, A. G. Bibiloni, J. Desimoni, and A. R. López-Garcia, Phys. Rev. B **34**, 2982 (1986).
[59] B. H. Christensen, K. Vestentoft, and P. Balling, Appl. Surf. Sci. **253**, 6347 (2007).
[60] American Institute of Physics, *American Institute of Physics Handbook* (McGraw-Hill, New York, 1957).
[61] P. Garoche and J. Bigot, Phys. Rev. B **28**, 6886 (1983).
[62] N. Inogamov and Y. V. Petrov, J. Exp. Theor. Phys. **110**, 446 (2010).
[63] D. N. Manh, D. Mayou, F. Cyrot-Lackmann, and A. Pasturel, J. Phys. F **17**, 1309 (1987).
[64] R. H. M. Groeneveld, R. Sprik, and A. Lagendijk, Phys. Rev. B **51**, 11433 (1995).
[65] P. D. Desai, H. M. James, and C. Y. Ho, J. Phys. Chem. Ref. Data **13**, 1097 (1984).
[66] Z. Lin, L. V. Zhigilei, and V. Celli, Phys. Rev. B **77**, 075133 (2008).
[67] W. McMillan, Phys. Rev. **167**, 331 (1968).
[68] P. B. Allen, in *Quantum Theory of Real Materials*, edited by J. R. Chelikowsky and S. G. Louie (Kluwer Academic Press, Boston, 1996).
[69] E. Pekarskaya, C. Kim, and W. Johnson, J. Mater. Res. **16**, 2513 (2001).
[70] B. Yang, M. L. Morrison, P. K. Liaw, R. A. Buchanan, G. Wang, C. T. Liu, and M. Denda, Appl. Phys. Lett. **86**, 141904 (2005).
[71] F. Shimizu, S. Ogata, and J. Li, Mater. Trans. **48**, 2923 (2007).